Eur. Phys. J. A (2017) **53**: 200
DOI 10.1140/epja/i2017-12391-5

**The European Physical Journal A**

Regular Article – Theoretical Physics

# Rotational structure of odd-proton $^{103,105,107,109,111}$Tc isotopes

Amit Kumar[1,2], Dhanvir Singh[1], Suram Singh[2], Arun Bharti[1,a], G.H. Bhat[2], and J.A. Sheikh[3]

[1] Department of Physics and Electronics, University of Jammu, Jammu-180006, India
[2] Department of Higher Education, Government of J&K, Jammu, India
[3] Department of Physics, University of Kashmir, Srinagar-190006, India

Received: 21 March 2017 / Revised: 29 August 2017

Communicated by F. Gulminelli

**Abstract.** A systematic study of the yrast band structure for the neutron-rich odd-mass $^{103-111}$Tc nuclei is carried out using Projected Shell Model. The rotational band structure has been studied up to a maximum spin of $59/2^+$. Excellent agreement with available experimental data for all isotopes is obtained. The energy spectra and electromagnetic transition strengths in terms of the configuration mixing of the angular-momentum projected multi-quasiparticle states are studied in detail. Signature splitting in the yrast rotational band is well described in the perspective of nuclear structure physics. The back-bending phenomenon is also well described for these nuclei in the present work.

## 1 Introduction

For neutron-rich $A \sim 100$ nuclei, the valence nucleons begin to fill the $h_{11/2}$ neutron and $g_{9/2}$ or $d_{5/2}$ proton orbitals. The nuclear structure in this mass region is very sensitive to the occupancy level of these single-particle configurations, which is illustrated by the rapid changes in nuclear spectroscopic properties as a function of both neutron and proton numbers. Sudden onset of quadrupole deformation in the Sr and Zr isotopes, the emerging $\gamma$ degree of freedom in the Mo-Ru region, and the predicted prolate to oblate shape transition in the Pd isotopes are certainly examples making this region quite interesting for its study. The anomalous behaviour of nuclear structure has made this region an ideal testing ground for various theoretical models [1–4].

Further, since the nuclei of this mass region lie far from the $\beta$-stability line, therefore, these nuclei have been at the forefront of nuclear structure research in the past. The odd-$A$ neutron-rich Tc isotopes with $Z = 43$ lie in this region with active $Z = 38$, 40 and $N = 56$ subshell closures. The presence of these subshell closures has a strong effect on the shapes and shape transition of these nuclei as well. The intrinsic configurations such as shape coexistence, and transitions in the neutron-rich nuclei with $Z > 40$, $N > 58$ have drawn much attention in the past. For the nuclei lying in the $A \sim 100$ mass region, it has been found that proton orbitals originating from the $\pi g_{9/2}$ subshell closest to the Fermi level are affected in special nuclear shapes ($\beta_2$) [2]. Neutron states from the $\nu h_{11/2}$ subshell strongly drive nuclei in this region to prolate deformation, since the neutron Fermi level is below or near the bottom of the $\nu h_{11/2}$ subshell. The existence of such interesting nuclear structure properties in Tc isotopes has attracted the attention of various research groups [5–12] in the past. Moreover, with the development in experimental techniques, a large amount of experimental data for these isotopes has been made available to test the applicability of various theoretical models. Thus, Tc isotopes lying in the $A \sim 100$ mass region are the best candidates to study in a suitable theoretical framework. As a first step, in the present work, an isotopic chain of odd-mass $^{103-111}$Tc nuclei has been taken up for its study in a microscopic theoretical approach known as Projected Shell Model (PSM), as this model has been found successful in the recent past [13–16] in describing the nuclear structure properties of nuclei lying in the mass region $A \sim 100$. Since the present work is focussed on the study of this isotopic chain, therefore, it becomes necessary to know about the type of research work carried out on these nuclei by various other research groups in the past. In this direction, a brief review of the research work carried out on odd-mass $^{103-111}$Tc isotopes in the past has been presented below.

A comprehensive study of level schemes of odd-mass $^{103-111}$Tc nuclei has been made in the past by means of various experimental techniques like spontaneous fission studies, fusion-evaporation reaction, gamma ray spectroscopy, thermal neutron-induced fission, $\beta$-decay, etc. [5–12]. High-spin structures in $^{103}$Tc have been identified for the first time by using the fusion reaction technique [5], whereas several $\gamma$ transitions in $^{105-109}$Tc nuclei were identified for the first time and a new level

---

[a] e-mail: `arunbharti_2003@yahoo.co.in` (corresponding author)

scheme was proposed for these nuclei from spontaneous fission studies [6]. The near yrast and medium spin structures of $^{107}$Tc and $^{109}$Tc have been re-investigated using $\gamma$-spectroscopy [7,8]. The known [9] level scheme of $^{111}$Tc has been further extended up to $33/2^+$ by Luo *et al.* [10] through the spontaneous fission technique. Also, based on the study of Tc isotopes, it has been reported that a weak coupling scheme, existing in lighter Tc isotopes, shifts towards a strong coupling scheme from $^{97}$Tc to $^{105}$Tc [5]. Further, it has also been confirmed [7,11,12] that this strong coupling scheme is also present in $^{107}$Tc and $^{109}$Tc. This evolution of coupling schemes has been interpreted as happening due to the location of the Fermi level which changes with deformation as the neutron number increases.

The main goal of the present research work is to investigate, in a phenomenological way, the structure of odd-$A$ $^{103-111}$Tc nuclei employing the quantum-mechanical framework known as Projected Shell Model (PSM), which can well describe the properties of deformed nuclei including energy levels, prediction of back-bending, signature splitting [17–19]. The PSM approach is based on the shell model philosophy in which a deformed (Nilsson type) single-particle basis is used and the pairing correlations are incorporated into the basis by a BCS calculation for the Nilsson states. Unlike shell model, PSM uses truncated configuration space which is one of its most important advantages. PSM not only describes the observed high spin data in a qualitative way but also is a handy tool to have an insight into the structure of the nuclei under study. The paper is organized as follows. In sect. 2, we outline the theory of PSM and also present the necessary requirements for the present calculations. In sect. 3, we present the description of research results of the present study. Comparison with the experimental data is also made in this section. Finally, the paper is summarized in sect. 4.

## 2 An outline of theory used

A PSM calculation [20,21] starts with the deformed Nilsson single-particle states [22]. Deformed states calculated in this way are defined in the intrinsic frame of reference in which the rotational symmetry is broken. In order to calculate the observables, it is necessary to restore the broken rotational symmetry in the wave functions. This can be achieved by using the standard angular-momentum projection method [23]. The projected states are then used to diagonalize a rotational invariant two-body shell model Hamiltonian. Thus, such a model follows closely the basic philosophy of the nuclear shell model. The main difference from the conventional shell model is that PSM starts with a deformed basis rather than a spherical one. The deformed basis is constructed by using the parameters $\kappa$ and $\mu$ [24] (given in table 1) in the Nilsson potential to reproduce the correct shell filling.

In the PSM, the rotationally invariant Hamiltonian is taken to be

$$\hat{H} = \hat{H}_0 - \frac{\chi}{2}\sum_{\mu}\hat{Q}^{\dagger}_{\mu}\hat{Q}_{\mu} - G_M\hat{P}^{\dagger}\hat{P} - G_Q\sum_{\mu}\hat{P}^{\dagger}_{\mu}\hat{P}_{\mu}, \quad (1)$$

**Table 1.** Set of Nilsson parameters used as input in the present calculations of $^{103-111}$Tc nuclei.

| Major shell | Protons | | Neutrons | |
|---|---|---|---|---|
| $N$ | $\kappa$ | $\mu$ | $\kappa$ | $\mu$ |
| 2 | 0.06741 | 0.56948 | – | – |
| 3 | 0.06741 | 0.56948 | 0.06392 | 0.47886 |
| 4 | 0.06741 | 0.56948 | 0.06392 | 0.47886 |
| 5 | – | – | 0.06392 | 0.47886 |

where the first term is the spherical single-particle energy and the remaining terms are quadrupole-quadrupole, monopole pairing, and quadrupole pairing interactions, respectively. In the present work, we have assumed that the deformed single particle states have axial symmetry and thus, the basis states, $|\varphi_k\rangle$, have $K$ as good quantum number, *i.e.*, the intrinsic states are the eigenstates of the $K$-quantum number.

After performing BCS calculation, deformed quasiparticle (*qp*) states are obtained from which the PSM basis can be constructed. The set of multi-quasiparticle states for configuration space is

$$\{|\varphi_k\rangle\} = \left\{a^{\dagger}_{\pi}|0\rangle,\ a^{\dagger}_{\pi}a^{\dagger}_{\upsilon_1}a^{\dagger}_{\upsilon_2}|0\rangle\right\}, \quad (2)$$

where $a^{\dagger}$'s are the *qp* creation operators, $\pi$'s ($\nu$'s) denote the proton (neutron) Nilsson quantum numbers which run over the low-lying orbitals, and $|0\rangle$ is the Nilsson + BCS vacuum (0-*qp* state). In eq. (2), the 3-*qp* states selected for the many-body basis are those consisting of the 1-*qp* proton state plus a pair of *qp*'s from nucleons of another kind (neutrons) and this selection is based on physical considerations. In general, 3-*qp* states made by three nucleons of the same kind are also allowed, but such states usually lie higher in energy. The inclusion of the 3-*qp* configurations is important for odd-mass nuclei for a description of the band-crossing phenomenon which is caused by a rotation alignment of a pair of quasi-neutrons.

These projected multi-quasiparticle states serve as the building blocks of PSM basis and the superposition of these states gives rise to the many-body wave function. Angular momentum projection transforms the wavefunction from intrinsic frame to laboratory frame. The total wave function is expressed as

$$|\Psi^{\sigma}_{IM}\rangle = \sum_{Kk} f^{\sigma}_{\kappa}\hat{P}^{I}_{MK}|\phi_{\kappa}\rangle, \quad (3)$$

where index $\sigma$ labels the states with the same angular momentum and $\kappa$ the basis states. $f^{\sigma}_{\kappa}$ are the weights of the basis state $\kappa$. Finally, the Hamiltonian is diagonalized in the projected states and the diagonalization determines $f^{\sigma}_{\kappa}$ in eq. (3). For more details, one can refer to the review articles on PSM [20,21].

Further, the $QQ$-force strength $\chi$ is determined through a self-consistent condition with a given quadrupole deformation $\varepsilon_2$. The hexadecapole deformation, $\varepsilon_4$, has also been included in the mean-field Nilsson potential to reproduce experimental energies correctly. The deformation parameters, $\varepsilon_2$ and $\varepsilon_4$, used in the present calculations are listed in table 2.

**Table 2.** Deformation and interaction parameters used as input in the present calculations of $^{103-111}$Tc nuclei.

| | $^{103}$Tc | $^{105}$Tc | $^{107}$Tc | $^{109}$Tc | $^{111}$Tc |
|---|---|---|---|---|---|
| $\varepsilon_2$ | 0.260 | 0.278 | 0.317 | 0.279 | 0.287 |
| $\varepsilon_4$ | 0.027 | 0.027 | 0.000 | 0.027 | 0.000 |
| $G_M/G_Q$ | 0.22 | 0.22 | 0.22 | 0.22 | 0.22 |

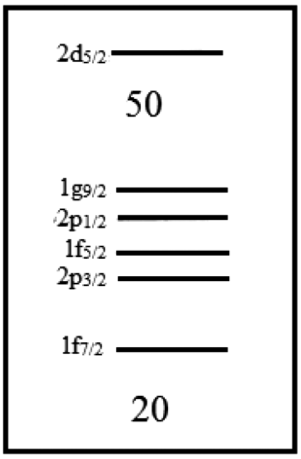

**Fig. 1.** Part of the Standard Shell Model diagram showing single-particle orbitals for protons used in this work, arbitrary units [31].

The monopole pairing strength $G_M$ is adjusted to give the known energy gaps and is of the form

$$G_M = \left( G_1 \mp G_2 \frac{N-Z}{A} \right) \frac{1}{A} \text{ (MeV)}, \tag{4}$$

with "−" for neutrons and "+" for protons. Here, $G_1$ and $G_2$ are the coupling constants which are adjusted to yield the known odd-even mass differences and in the present calculations, these are taken as 19.70 and 10.00, respectively. The quadrupole pairing strength $G_Q$ is assumed to be proportional to $G_M$, with the proportionality constant being fixed as 0.22 for the present calculations. In these calculations, the configuration space consists of three major shells for each kind of nucleon: $N = 2$, 3 and 4, for protons and $N = 3$, 4 and 5, for neutrons and to truncate the valence space, an energy window of 3.5 MeV is chosen around the Fermi surface. The present calculations are carried by employing the same set of input parameters for all the isotopes under study.

## 3 Results of calculations and comparison with experimental data

As can be seen from the standard shell model schematic diagram (fig. 1), there are five single particle proton orbits in the 20–50 major shell, four of which with negative parity, which are $1f_{7/2}$, $1f_{5/2}$, $2p_{3/2}$ and $2p_{1/2}$, and one with positive-parity, which is $1g_{9/2}$. It is well known that for the nuclei having proton number larger than 40, the $2d_{5/2}$ proton orbit from the upper shell becomes lower in energy and creates an opportunity for the particle to occupy this orbit energetically. Hence, in the present PSM calculations for odd-$A$ Tc isotopes, the single particle proton orbits, $2d_{5/2}$ and $1g_{9/2}$, are taken into account.

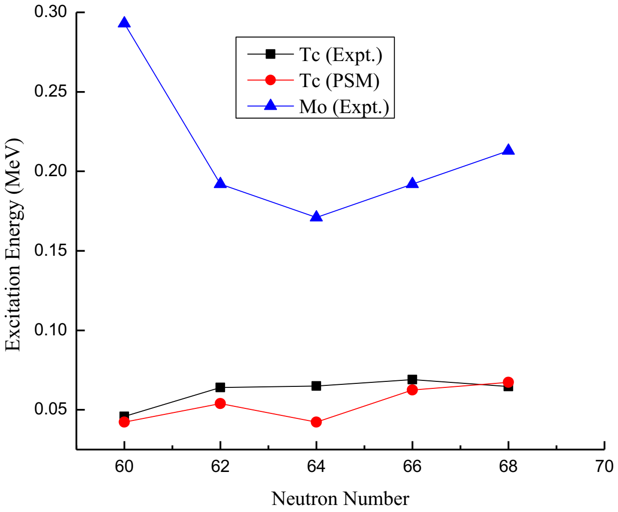

**Fig. 2.** Variation of the observed excitation energy of first excited state (${E_2}^+$) in the even-even $^{102-110}$Mo isotopes and comparison of excitation energy of the first excited state (${E_{7/2}}^+$) of the yrast band in odd-mass $^{103-111}$Tc isotopes with the inclusion of the $2d_{5/2}$ proton orbit.

In order to see the effect of the inclusion of the $2d_{5/2}$ orbit in the present PSM calculations, we have plotted the calculated results of the energy of the first excited state (${E_{7/2}}^+$) of odd-$A$ $^{103-111}$Tc nuclei along with its experimental counterpart in fig. 2. The comparison shows a satisfactory agreement between the two forms of data. Besides this, in the same figure, we have also plotted the experimental data of the energy of the first excited state (${E_2}^+$) of the even-even $^{102-110}$Mo [25–29] nuclei lying in the same mass region, where the experimental data is based on $1g_{9/2}$ proton orbital as the intruder level and it does not involve $2d_{5/2}$ proton orbit. It is very much clear from fig. 2 that the energy of the first excited states of even-even $^{102-110}$Mo isotopes (with $1g_{9/2}$ as intruder level) is very high and when one proton is added to these Mo nuclei ($Z = 42$), the energy of the first excited state of the resultant nuclei, *i.e.*, $^{103-111}$Tc ($Z = 43$) gets reduced, thereby giving rise to the appearance of collectivity in Tc isotopes. It is also very well known from the Grodzin rule [30] that the nuclei with the least value of energy of the first excited state are more deformed and there arises a phenomenon of collectivity in these nuclei. Further, the effect of inclusion of the $2d_{5/2}$ proton orbit on the results of energy and electromagnetic transitions for odd-mass $^{97-103}$Tc isotopes is already investigated successfully by Dejbakhsh and Shlomo [31] using IBFM-2 [32] and with this aim in mind, an attempt is made in the present work to achieve this successful result for odd-mass $^{103-111}$Tc isotopes by using PSM framework of calculations.

### 3.1 Projected quasiparticle configuration and configuration mixing

The physics of multi-quasiparticle states is well incorporated in the PSM framework. The PSM follows closely the shell model philosophy, and in fact, is a shell model constructed in a deformed multi-quasiparticle basis. More precisely, in the PSM, angular-momentum–projected multi-quasiparticle configurations form a shell model basis in which a two-body Hamiltonian is diagonalized. The energy of a theoretical band $\kappa$ is defined by

$$E_\kappa(I) = \frac{\langle \phi_\kappa | \hat{H} \hat{P}^I_{KK} | \phi_\kappa \rangle}{\langle \phi_\kappa | \hat{P}^I_{KK} | \phi_\kappa \rangle}, \tag{5}$$

which can be plotted as a function of spin for various bands and important physics can be drawn from these plots, which are generally known as band diagrams. Here, $\hat{P}^I_{KK}$ is the angular-momentum projection operator.

The configurations of various energy bands are constructed from the well-established Nilsson model by taking those deformed Nilsson single-particle states which are near the Fermi levels. Each configuration usually corresponds to a real observable state, and in most cases is the dominant component in the wave function of an observed state. In other words, the configuration space, commonly with less than one hundred projected multi-quasiparticle states, spans a shell model basis in which one can discuss physics even before diagonalization. This is a very pleasant feature of the PSM.

In fig. 3, we plot the relevant 1-*qp* and 3-*qp* bands in $^{103-111}$Tc, whose configurations are given in the same figure. For $^{103}$Tc (fig. 3(a)), it is seen that at low spins the 1-*qp* band $1\pi d_{5/2}$ [5/2], $K = 5/2$ forms the yrast states. However, as spin increases, it is approached by several other bands, as can be seen in fig. 3(a). At spin the $25/2^+$, the two 3-*qp* bands $1\pi d_{5/2}$ $[5/2] + 2\nu h_{11/2}$ $[-3/2, 5/2]$, $K = 7/2$ and $1\pi d_{5/2}$ $[-3/2] + 2\nu h_{11/2}$ $[1/2, -3/2]$, $K = -5/2$, come closer to the above-mentioned 1-*qp* band and band crossing occurs. These interacting 3-*qp* bands, thus contribute to the formation of the yrast states up to the spin of $39/2^+$. Afterwards, another 3-*qp* band identified as $1\pi d_{5/2}$ $[-3/2] + 2\nu h_{11/2}$ $[-3/2, 5/2]$, $K = -1/2$ joins the above mentioned bands, which then together result in the formation of yrast states up to the last calculated spin.

For $^{105}$Tc, it is clear from fig. 3(b) that the yrast states at low spins are dominated by the 1-*qp* band $1\pi d_{5/2}$ [5/2], $K = 5/2$. However, it is seen in fig. 3(b) that, at spin $I = 27/2^+$, this configuration is strongly disturbed by another nearby 3-*qp* band $1\pi d_{5/2}$ $[5/2]+2\nu h_{11/2}$ $[-3/2, 5/2]$, $K = 7/2$, which crosses the above-mentioned 1-*qp* band and forms the yrast states up to the spin of $41/2^+$. At spin $41/2^+$, this 3-*qp* band starts interacting with two more 3-*qp* bands identified as $1\pi d_{5/2}$ $[-3/2]+2\nu h_{11/2}$ $[-3/2, 5/2]$, $K = -1/2$ and $1\pi g_{9/2}$ $[1/2]+2\nu h_{11/2}$ $[-3/2, 5/2]$, $K = 3/2$ and combination of these interacting bands results in the formation of the yrast band till the last calculated spin.

The low spin yrast states of $^{107}$Tc, as shown in fig. 3(c), are dominated by a mixture of two 1-*qp* bands identified as $1\pi d_{5/2}$ [5/2], $K = 5/2$ and $1\pi d_{5/2}$ [1/2], $K = 1/2$. This combination continues to form the yrast states until the band crossing occurs at $39/2^+$, where it is crossed by a 3-*qp* band $1\pi d_{5/2}$ $[1/2]+2\nu h_{11/2}$ $[-3/2, 5/2]$, $K = 3/2$. After this spin, this 3-*qp* band gets overlapped with another 3-*qp* band $1\pi d_{5/2}$ $[-3/2] + 2\nu h_{11/2}$ $[-3/2, 5/2]$, $K = -1/2$ and their combination leads to the formation of yrast spectra up to the last calculated spin.

In the case of $^{109}$Tc (see fig. 3(d)), up to the spin of $35/2^+$, the yrast spectrum is formed by a 1-*qp* band $1\pi d_{5/2}$ [5/2], $K = 5/2$. At the spin of $35/2^+$, band crossing occurs and a 3-*qp* band having configuration $1\pi d_{5/2}$ $[5/2] + 2\nu h_{11/2}$ $[-3/2, 5/2]$, $K = 7/2$ crosses the above-mentioned 1-*qp* band. Further, this 3-*qp* band interacts with two more 3-*qp* bands, which are identified as $1\pi d_{5/2}$ $[-3/2] + 2\nu h_{11/2}$ $[5/2, -7/2]$, $K = -5/2$ and $1\pi d_{5/2}$ $[-3/2]+2\nu h_{11/2}$ $[-3/2, 5/2]$, $K = -1/2$, and these bands contribute to the formation of yrast spectra up to the last calculated spin.

Finally, for $^{111}$Tc (fig. 3(e)), the dominated bands at low spins are $1\pi d_{5/2}$ [5/2], $K = 5/2$; $1\pi d_{5/2}$ [1/2], $K = 1/2$ and their mixture forms yrast states up to spin $33/2^+$. This mixture of 1-*qp* bands gets crossed by a 3-*qp* band identified as $1\pi d_{5/2}$ $[-3/2]+2\nu h_{11/2}$ $[5/2, -7/2]$, $K = -5/2$ and forms the yrast spectra up to spin $45/2^+$. Afterwards, this band starts interacting with another 3-*qp* band $1\pi d_{5/2}$ $[1/2] + 2\nu h_{11/2}$ $[5/2, -7/2]$, $K = -1/2$ and these two interacting bands contribute to the yrast spectra for the rest of the calculated spins.

In fig. 4, we present the rotational yrast band of odd-mass $^{103-111}$Tc nuclei obtained after configuration mixing in the present PSM calculations. The yrast band is the band with the lowest energy states for a given angular momentum, no matter which band the angular momentum state belongs to. The PSM results on the energy of the yrast band are plotted against the spin for the $^{103-111}$Tc isotopes in figs. 4(a)–(e). Further, in order to show the efficacy of the applied PSM for the chosen set of nuclei, we have also compared these theoretical results of the yrast spectra with the available experimental data [5–10, 33–37] for all odd-mass $^{103-111}$Tc nuclei in the same figures. It is pertinent to mention here that the experimental data for $^{103,105}$Tc isotopes is sparse and is available only up to the maximum spin of $17/2^+$ and in the case of $^{107,109,111}$Tc the experimental data is available up to a maximum spin of $33/2^+$. Nevertheless, we have presented the theoretical results up to the maximum spin value of $59/2^+$ in figs. 4(a)–(e). Further, the PSM results are found to be in excellent agreement with the amount of available experimental data. One interesting feature that has emerged from the present calculations for $^{103-111}$Tc is that the band head spin value has been obtained as $5/2^+$, which is the same as shown by the experimental data [5–10, 33–37] and, thus, the band head spin has been successfully reproduced by the present set of calculations.

To conclude, the available experimental yrast levels in $^{103-111}$Tc have been reproduced quite well by the present PSM calculations and the overall agreement can be considered to be satisfactory in all the odd-mass $^{103-111}$Tc isotopes.

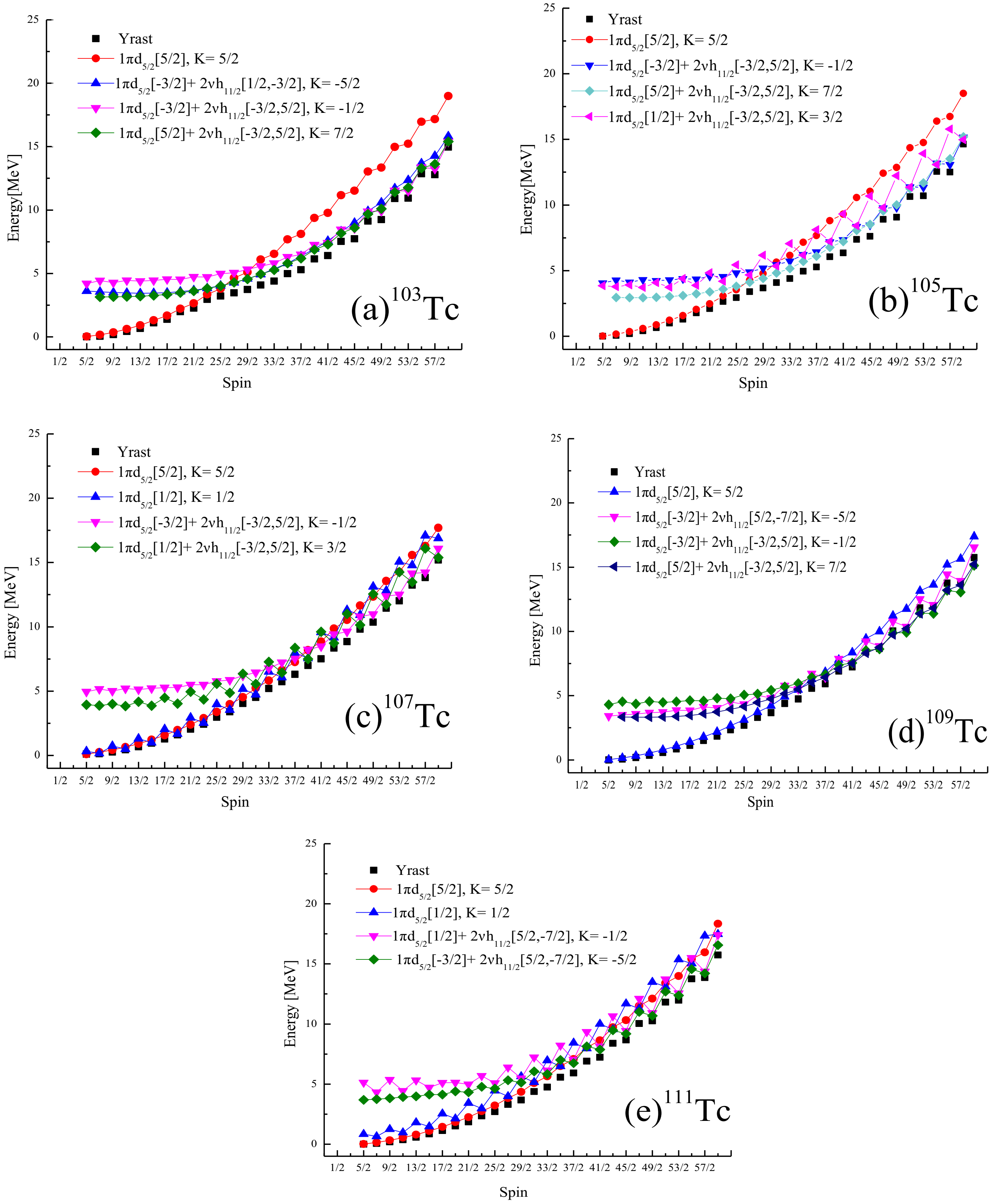

**Fig. 3.** Band diagrams of (a) $^{103}$Tc, (b) $^{105}$Tc, (c) $^{107}$Tc (d) $^{109}$Tc and (e) $^{111}$Tc. Only the important lowest lying bands in each configuration are plotted. The yrast band is also shown (filled squares).

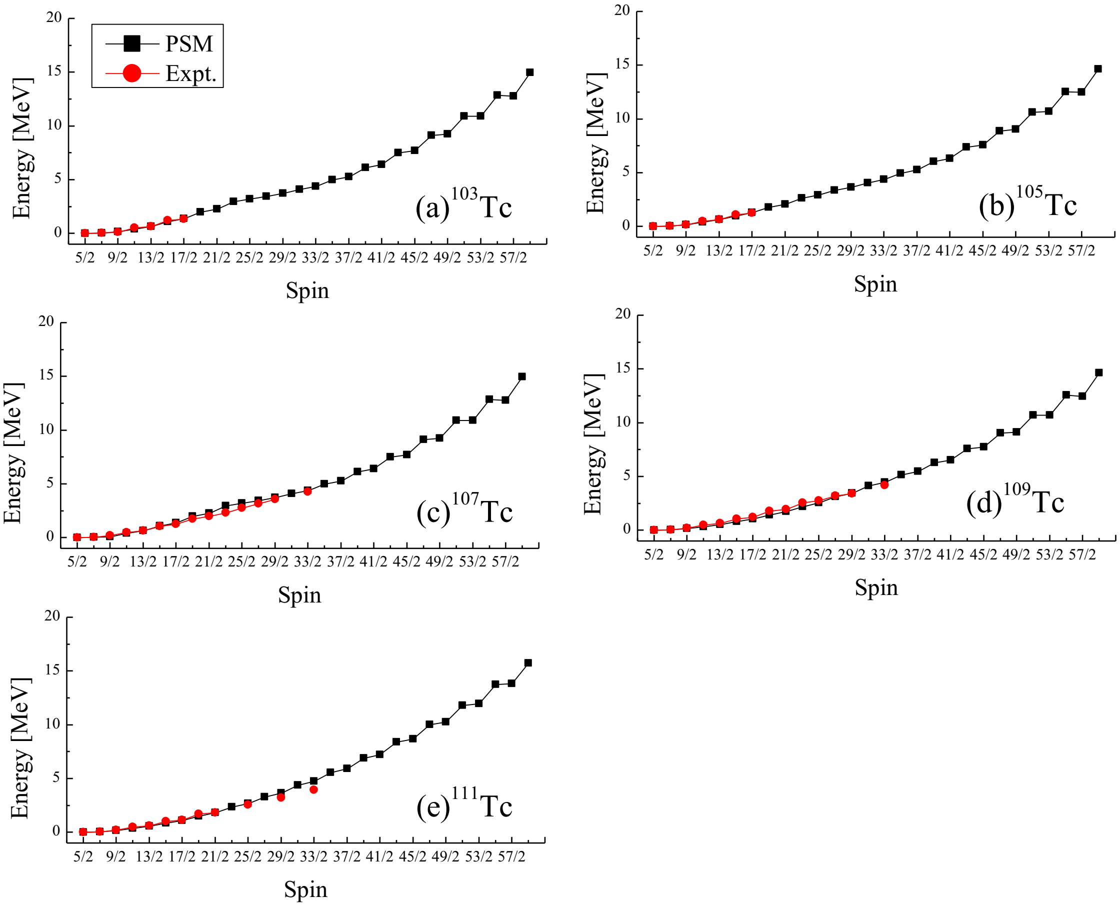

**Fig. 4.** Calculated positive-parity yrast band energies (PSM) in comparison with the available experimental data for (a) $^{103}$Tc, (b) $^{105}$Tc, (c) $^{107}$Tc (d) $^{109}$Tc and (e) $^{111}$Tc. The experimental data are taken from refs. [5–10,33–37].

## 3.2 Properties of the yrast band

In this section, we present the discussion about the properties of the rotational yrast band of odd-mass $^{103-111}$Tc nuclei. This rotational yrast band is obtained after configuration mixing in the PSM calculations and is based on the $\pi 2d_{5/2} \otimes \nu h_{11/2}$ configuration.

### 3.2.1 Kinetic and dynamical moments of inertia

It is well known that the moment of inertia is sensitive to nuclear properties, like the pairing strength and the specific orbitals active at the Fermi surface. A systematic analysis of the moments of inertia of a number of nuclei can, therefore, provide valuable information on such properties in these nuclei. As moment of inertia depends upon the angular momentum, therefore its variation can impart some valuable information about the change in nuclear structure. It can be represented as a plot between twice the kinetic moment of inertia and square of corresponding rotational frequencies and this plot gives the information about the back-bending phenomenon.

As it has been discussed in the previous sect. 3.1, that the structure of the nuclei changes at the value of angular momentum at which band crossing takes place, therefore, due to band crossing, the yrast line jumps from a given angular momentum with a small deformation to a higher angular momentum with a large deformation and results in a drastic increase in the moment of inertia at this angular momentum.

The back-bending in moment of inertia, observed in the rotational spectra of deformed nuclei, carries important information on the interplay between the ground band and bands with alignment of a pair of quasiparticles. Thus, an yrast sequence is formed by states of both of these bands such that the lower spin states are mainly of the ground band, and the major component of the higher spin states belongs to the bands with aligned quasiparticles. In figs. 5 and 6, we have plotted twice the kinetic moment of inertia ($2\Im^{(1)}$) as a function of the square of the rotational frequency ($\hbar^2\omega^2$) and the dynamical moment of inertia ($\Im^{(2)}$) as a function of the rotational frequency ($\hbar\omega$), respectively. A comparison of the PSM results with experimental data for the $^{103-111}$Tc isotopes

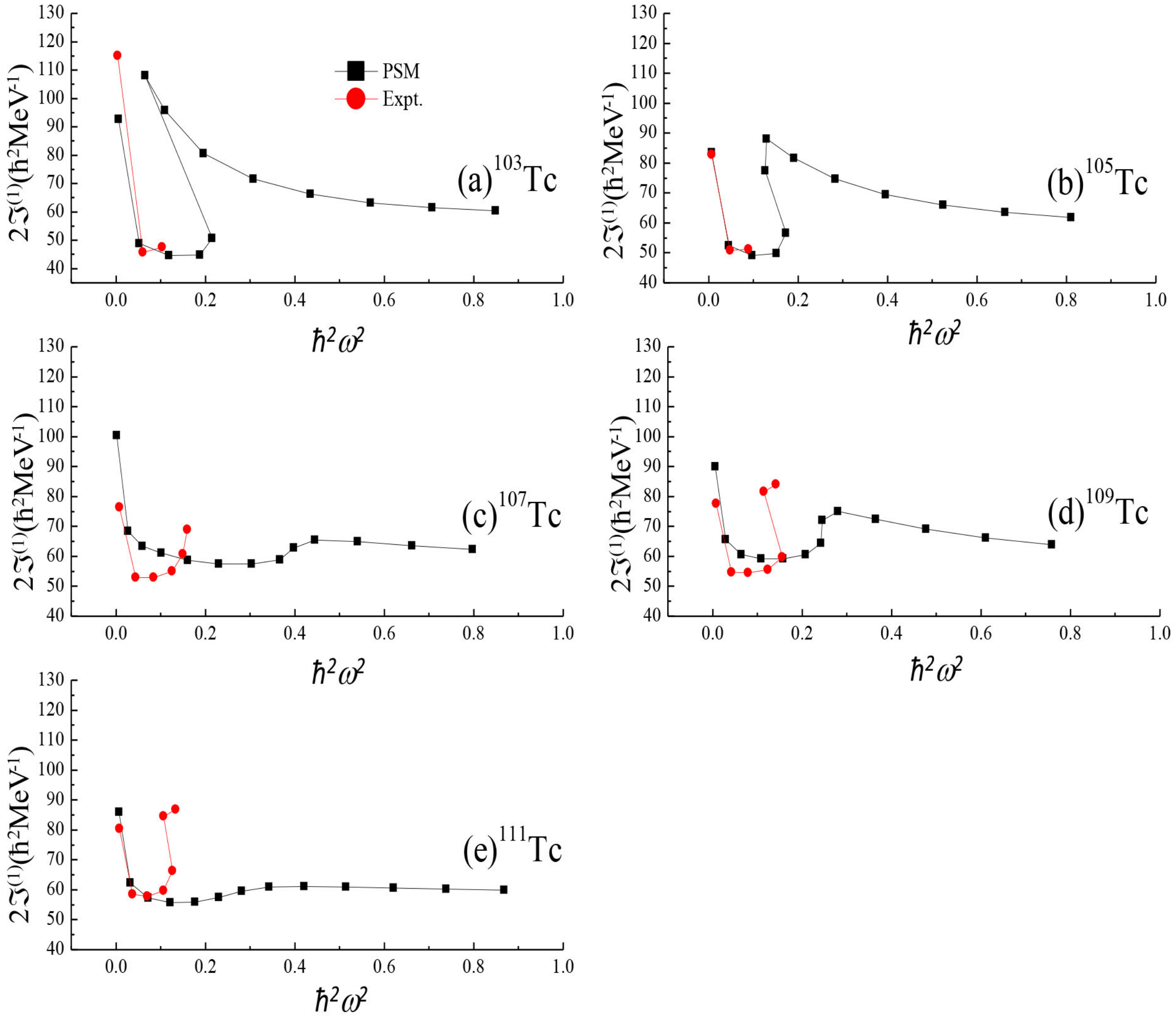

**Fig. 5.** The PSM results for twice the kinetic moment of inertia ($2\Im^{(1)}(\hbar^2\,\mathrm{MeV}^{-1})$) plotted against the angular frequency squared ($\hbar^2\omega^2$) for (a) $^{103}$Tc, (b) $^{105}$Tc, (c) $^{107}$Tc (d) $^{109}$Tc and (e) $^{111}$Tc. The experimental data [5–10,33–37] are also shown for comparison.

is also made in these figures. These quantities are defined as [38]

$$2\Im^{(1)} = \frac{(2I-1)}{\omega}, \qquad (6)$$

$$\Im^{(2)} = \frac{4}{E_\gamma(I) - E_\gamma(I-2)}, \qquad (7)$$

$$\hbar\omega = \frac{E_\gamma}{\sqrt{(I+1)(I+2)-K^2} - \sqrt{(I-1)I-K^2}}, \qquad (8)$$

where $E_\gamma = E(I) - E(I-2)$.

It is quite noteworthy from fig. 5 that the comparison between theory and experiment is overall satisfactory. The available experimental values of kinetic moments of inertia ($\Im^{(1)}$) are very well reproduced for $^{103,105}$Tc isotopes. Further, the results of PSM calculations on $^{103}$Tc (fig. 5(a)) and $^{105}$Tc (fig. 5(b)) have predicted back-bending at the spin $25/2^+$ in both of these nuclei at frequencies 0.2142 $\hbar^2\omega^2$ and 0.1720 $\hbar^2\omega^2$, respectively, but this feature is not reflected by the experiments due to scarcity of data. Whereas, for $^{107}$Tc, the experimental data is showing an up-bending at the spin $I = 25/2^+$ corresponding to the frequency 0.15 $\hbar^2\omega^2$, the theoretical data reflects this feature to be less pronounced at a delayed frequency 0.36 $\hbar^2\omega^2$. For $^{109}$Tc (fig. 5(d)) and $^{111}$Tc (fig. 5(e)), both theoretical and experimental results show the phenomenon of up-bending at the same spin $I = 25/2^+$, however, the theoretical one is not as sharp as the experimental one but the trend is the same.

To conclude, the predicted back-bending and up-bending in $^{103-111}$Tc nuclei can be attributed to the crossing of the ground band, *i.e.*, the 1-*qp* band consisting of a single proton ($\pi d_{5/2}$) with another 3-*qp* rotational band consisting of one proton and two neutrons ($1\pi d_{5/2} + 2\upsilon h_{11/2}$) having larger moment of inertia. Further, since the back-bending is also known to arise due to the breaking of a neutron pair from high-$j$ orbital and in the present PSM calculations, the high-$j$ orbital is $h_{11/2}$, therefore, the

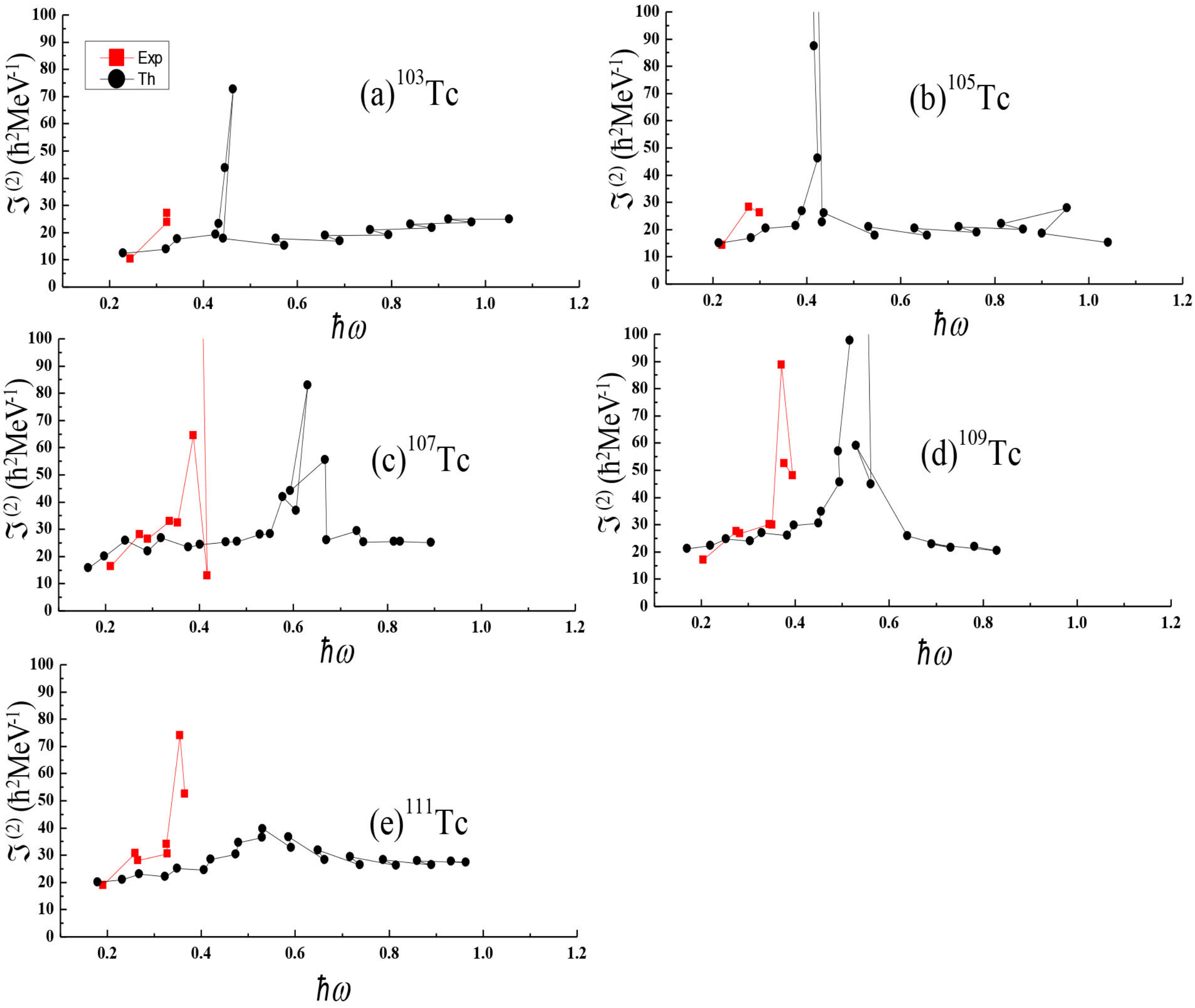

**Fig. 6.** The PSM results for the dynamical moment of inertia ($\Im^{(2)}(\hbar^2\,\mathrm{MeV}^{-1})$) plotted against the angular frequency ($\hbar\omega$) for (a) $^{103}$Tc, (b) $^{105}$Tc, (c) $^{107}$Tc (d) $^{109}$Tc and (e) $^{111}$Tc. The experimental data [5–10,33–37] are also shown for comparison.

arise of back-bending could also be thought as being happening due to the breaking of a neutron pair from $h_{11/2}$ orbital.

The dynamical moment of inertia is very sensitive to changes in the structure as nuclei rotate and this quantity represents a direct impact of the kinetic moment of inertia as it describes the variation of the kinetic moment of inertia. In figs. 6(a)–(e), we have plotted the PSM results along with their experimental counterparts for dynamical moment of inertia $\mathfrak{I}^{(2)}$ as a function of rotational frequency ($\hbar\omega$). These results are correctly explaining the phenomenon of back-bending or up-bending reflected by the kinetic moment of inertia $\mathfrak{I}^{(1)}$ plotted as a function of the square of the rotational frequency ($\hbar^2\omega^2$) in fig. 5. For example, in $^{103}$Tc and $^{105}$Tc, the change of $\mathfrak{I}^{(2)}$ is predicted to occur at $\hbar\omega \approx 0.45\,\mathrm{MeV}$ and 0.42 MeV, respectively, while the experimental data do not show any sign of discontinuity in the variation of $\mathfrak{I}^{(2)}$ due to the non-availability of the data for high spin states for these two isotopes. Moreover, the change of $\mathfrak{I}^{(2)}$ in $^{103}$Tc and $^{105}$Tc is found to occur at the same spin ($25/2^+$) corresponding to which PSM results have predicted back-bending in these two isotopes, as shown in figs. 5(a) and 5(b). In the case of $^{107}$Tc, the change of $\mathfrak{I}^{(2)}$ is observed at $\hbar\omega \approx 0.4\,\mathrm{MeV}$ while PSM results have predicted this change at $\hbar\omega \approx 0.6\,\mathrm{MeV}$. Though these values of rotational frequency are not close to each other, the delayed change of $\mathfrak{I}^{(2)}$ is in accordance with the delayed up-bending shown by PSM results for kinetic moment of inertia in $^{107}$Tc (see fig. 5(c)). For $^{109}$Tc, the PSM results on $\mathfrak{I}^{(2)}$ have reflected a discontinuity at $\hbar\omega \approx 0.5\,\mathrm{MeV}$ while, experimentally, it is found to take place at $\hbar\omega \approx 0.4\,\mathrm{MeV}$, which still can be considered as a good agreement between two forms of the data on the variation of the dynamical moment of inertia with the rotational frequency. For $^{111}$Tc, the PSM predicts a very slow and less pronounced change of $\mathfrak{I}^{(2)}$ at around $\hbar\omega \approx 0.4\,\mathrm{MeV}$ while experimentally, it occurs at around $\hbar\omega \approx 0.35\,\mathrm{MeV}$ and this can be considered as a very good agreement with experiment.

From the above discussion on the results of dynamical moment of inertia $\mathfrak{I}^{(2)}$ in $^{103-111}$Tc isotopes, it can be concluded that the change of $\mathfrak{I}^{(2)}$ is predicted to occur around those values of rotational frequency ($\hbar\omega$) which are very close to experimental ones, except in $^{103,105}$Tc where experimental data do not show this feature due to the non-availability of data for higher spins. Moreover, it is also very much clear from the plots (see figs. 6(a)–(e)) that change of $\mathfrak{I}^{(2)}$ is found to occur at those values of spins corresponding to which the kinetic moment of inertia $\mathfrak{I}^{(1)}$ has shown a sign of the presence of back-bending or up-bending in $^{103-111}$Tc isotopes and thus the dynamical moment of inertia successfully describes the variation of $\mathfrak{I}^{(1)}$ in these isotopes.

### 3.2.2 Reduced transition probabilities

Reduced transition probabilities $B(E2)$ is a measure of collectivity and can give important information on the nuclear structure, thereby enhancing our knowledge of nuclear structure. Electromagnetic properties play an instrumental role in the critical evaluation of various models. The reduced electric quadrupole transition probability $B(E2)$ from an initial state ($I_i = I$) to a final state ($I_f = I - 2$) is represented by

$$B(E2, I_i \rightarrow I_f) = \frac{e^2}{2I_i + 1} |\langle \sigma_f, I_f || \hat{Q}_2 || \sigma_i, I_i \rangle|^2. \qquad (9)$$

Here, the operator $\hat{Q}_2$ is related to the quadrupole operators. In order to calculate $B(E2)$ values, the numerical values for proton (neutron) effective charges, as $e_\pi$ ($e_\nu$), have been employed, which are defined as

$$e_\pi = 1 + e_{eff} \quad \text{and} \quad e_\upsilon = e_{eff}$$

and in the present set of calculations we have taken $e_{eff} = 0.6$.

Similarly, one can also calculate the reduced magnetic transition probability $B(M1)$ by using PSM wave functions. Magnetic dipole transition strengths are sensitive to the single-particle nuclear wave function. The reduced magnetic dipole transition probability $B(M1)$ from the initial state ($I_i = I$) to the final state ($I_f = I - 1$) is calculated by using the following equation:

$$B(M1, I_i \rightarrow I_f) = \frac{\mu_N^2}{2I_i + 1} |\langle \sigma_f, I_f || \hat{M}_1 || \sigma_i, I_i \rangle|^2, \qquad (10)$$

where, the magnetic dipole operator $M_1$ is given by the following relation:

$$\hat{M}_1^\tau = g_l^\tau \hat{j}^\tau + (g_s^\tau - g_l^\tau)\, \hat{s}^\tau.$$

Here $\tau$ is either $\pi$ or $\nu$; $g_l$ and $g_s$ are the orbital and the spin gyromagnetic factors, respectively, and are defined as

$$\begin{aligned} g_\tau(\sigma, I) = \frac{1}{[I(I+1)(2I+1)]^{1/2}} &(g_l^\tau \langle \sigma, I \| J^\tau \| \sigma, I \rangle \\ &+ (g_s^\tau - g_l^\tau) \langle \sigma, I \| S^\tau \| \sigma, I \rangle) \qquad (11) \end{aligned}$$

and in these calculations, we take the free values for $g_l$, whereas for $g_s$, the free values are damped by a factor of 0.85. The standard free values of $g_l$ and $g_s$ for protons and neutrons are

$$g_l^\pi = 1, \quad g_l^\nu = 0, \quad g_s^\pi = 5.586 \times 0.85, \quad g_s^\nu = -3.826 \times 0.85.$$

In these calculations, the effective charges as well as damping of free values of $g_s$ have been used to take into account the effect of core-polarization and meson-exchange current corrections.

The reduced matrix element of an operator $\hat{O}$ ($\hat{O}$ is either $\hat{Q}$ or $\hat{M}$) is written by

$$\begin{aligned} \langle \sigma_f, I_f \| \hat{O}_L \| \sigma_i, I_i \rangle = &\sum_{\kappa_i, \kappa_f} f_{I_i \kappa_i}^{\sigma_i} f_{I_f \kappa_f}^{\sigma_f} \\ &\times \sum_{M_i, M_f, M} (-1)^{I_f - M_f} \begin{pmatrix} I_f & L & I_i \\ -M_f & M & M_i \end{pmatrix} \\ &\times \langle \phi_{\kappa_f} | \hat{P}_{K_{\kappa_f} M_f}^{I_f} \hat{O}_{LM} \hat{P}_{K_{\kappa_i} M_i}^{I_i} | \phi_{\kappa_i} \rangle. \quad (12) \end{aligned}$$

Figure 7 represents the calculated values of the reduced electric transition probabilities, ($B(E2)$) for positive-parity yrast band in $^{103-111}$Tc isotopes, whereas, the calculated data for magnetic transition probabilities ($B(M1)$) for positive-parity yrast bands in these isotopes have been presented in fig. 8. As no experimental data on $B(E2)$ and $B(M1)$ values are available for yrast bands on these nuclei, so one cannot make any comment on their degree of accuracy. However, these results could serve as motivation for experimentalists to look for this data.

Furthermore, in the present work, we have calculated the electromagnetic transition strength ratio ($B(M1)/B(E2)$) using the PSM wave functions for $^{103-111}$Tc nuclei. The experimental values of transition strength ratios are extracted from the measured intensities [33–37] using the relation given in ref. [39]. Figure 9 shows the comparison of experimental and calculated values of $B(M1)/B(E2)$ for the positive-parity yrast band for odd-mass $^{103-111}$Tc isotopes. Except for some transitions, most of the theoretical $B(M1)/B(E2)$ values appear to agree with the measured values. The spin dependence in the form of staggering $B(M1)/B(E2)$ ratios within the yrast band is correctly predicted by PSM calculations. This staggering pattern of $B(M1)/B(E2)$ may be occurring due to the presence of signature splitting in the yrast band which is also experimentally observed for these nuclei and discussed in the next section.

### 3.2.3 Staggering in yrast band

Another important property that is found in the $A \sim 100$ region is signature splitting. The spin dependence of $B(M1)/B(E2)$ ratio within the yrast states indicates the presence of signature splitting in odd-even $^{103-113}$Tc isotopes. In order to investigate the presence of staggering, we have calculated the quantity $S(I)$ [40], known as signature splitting function, which is often used to check the presence of staggering. In fig. 10, we have plotted $S(I)$ against spin up to $I = 59/2^+$ for $^{103-111}$Tc isotopes.

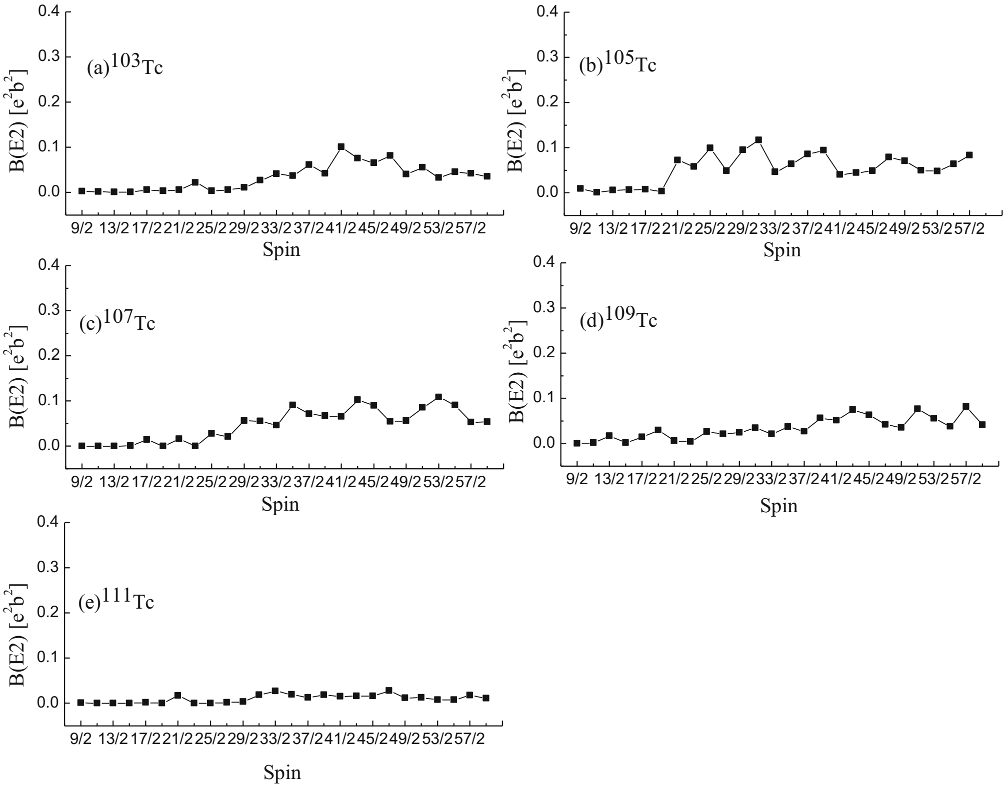

**Fig. 7.** Calculated $B(E2)$ transition probabilities for the positive-parity yrast bands in (a) $^{103}$Tc, (b) $^{105}$Tc, (c) $^{107}$Tc (d) $^{109}$Tc and (e) $^{111}$Tc.

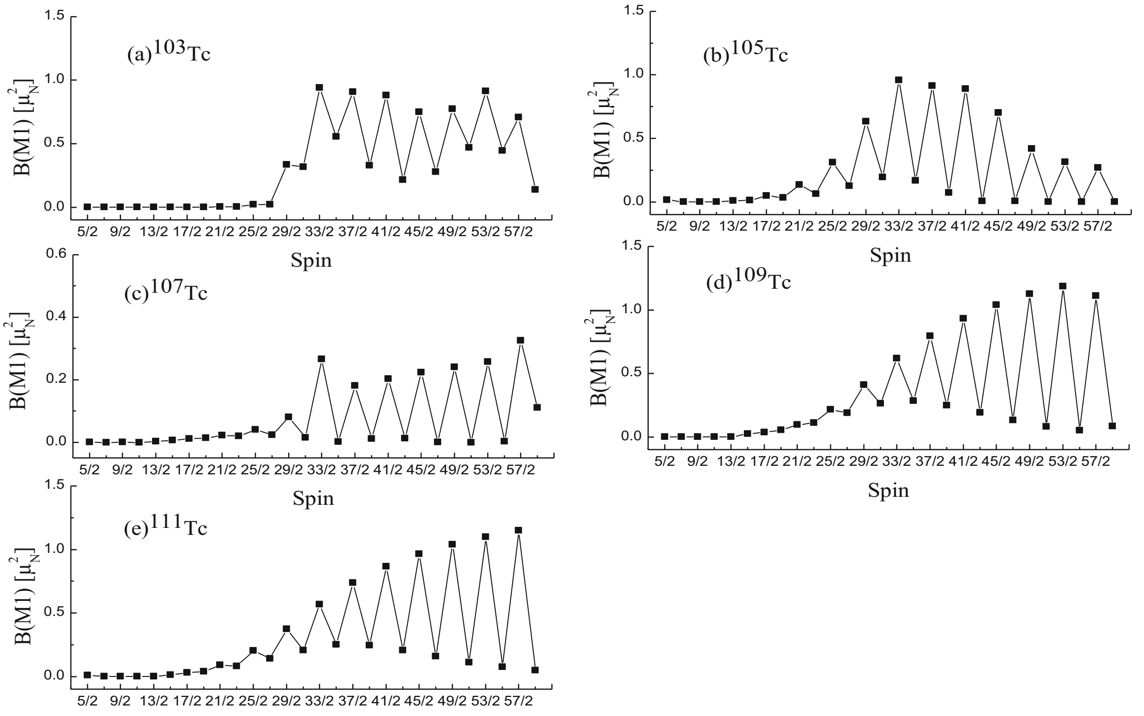

**Fig. 8.** Calculated $B(M1)$ transition probabilities for the positive-parity yrast bands in (a) $^{103}$Tc, (b) $^{105}$Tc, (c) $^{107}$Tc, (d) $^{109}$Tc, and (e) $^{111}$Tc.

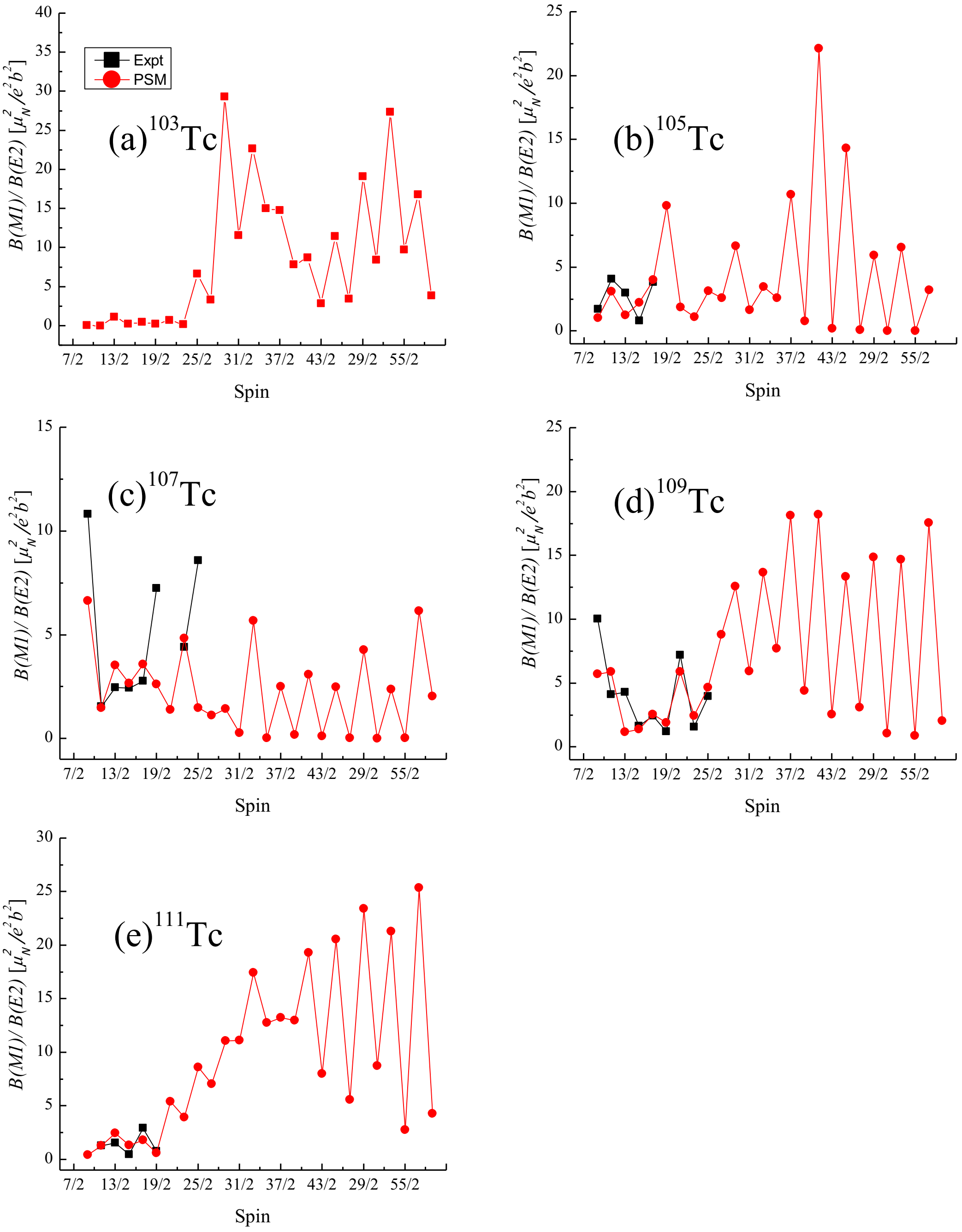

**Fig. 9.** Comparison of calculated $B(M1)/B(E2)$ transition strengths ratios with the experimental values obtained from the measured intensity of transitions for positive-parity bands in (a) $^{103}$Tc, (b) $^{105}$Tc, (c) $^{107}$Tc (d) $^{109}$Tc and (e) $^{111}$Tc. The experimental data are taken from refs. [33], [34], [35], [36] and [37] for $^{103}$Tc, $^{105}$Tc, $^{107}$Tc, $^{109}$Tc, and $^{111}$Tc, respectively.

Though the PSM data is not in good agreement with the available experimental counterpart, this figure clearly depicts that the experimentally observed staggering is quite reasonably reproduced by the present PSM calculations for positive-parity bands, as the trend of the experimental staggering is almost the same as that of PSM data. A little deviation found in the PSM data could be due to the presence of triaxiality in these Tc isotopes [10], since the present set of calculations have been performed with the axial PSM and the inclusion of triaxial degree of freedom in the applied framework may show some improvement in the data. It is very encouraging that the present model, with rather crude approximations, successfully reproduces experimental features related to the signature splitting in the yrast band described in this paper.

Now, the appearance of the staggering pattern of $B(M1)/B(E2)$ ratio in odd-$A$ $^{103-111}$Tc isotopes could also be related with the nature of different bands shown in the band diagram (fig. 3). It is clear that the bands forming the yrast spectra are not showing a smooth nature but

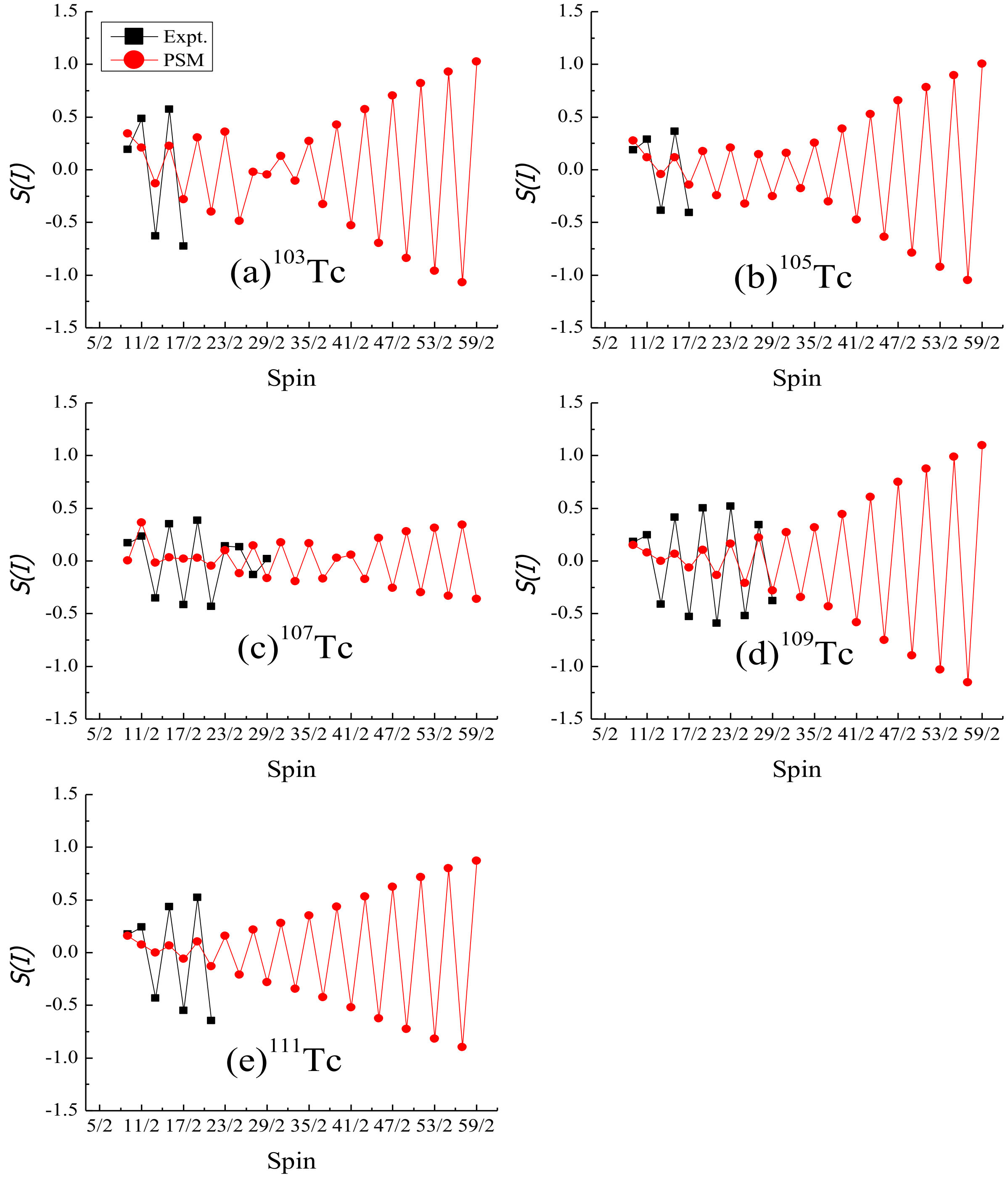

**Fig. 10.** Plots of signature splitting function $S(I)$ *versus* spins for (a) $^{103}$Tc, (b) $^{105}$Tc, (c) $^{107}$Tc, (d) $^{109}$Tc and (e) $^{111}$Tc. The experimental data are taken from refs. [5–10, 33–37].

have rather a zig-zag behaviour and the yrast states are formed by a mixture of multi-quasiparticle bands instead of a single 1-*qp* band. One can see from the band diagrams that, out of the all unperturbed bands taken in the diagonalization, only a few of them show energy staggering (the so-called signature splitting) and have a zig-zag behaviour as a function of spin. These unperturbed bands, which show staggering, influence the yrast states through the band mixing. Also, they dive down to the yrast region at higher spins, and therefore, bring strong energy staggering to the yrast band. It is thus the configuration mixing that nicely produces the observed signature splitting. The bands which are responsible for bringing staggering in these nuclei are those which have the low-$K$ values. In the present PSM calculations, we have identified that, in $^{103}$Tc, $^{105}$Tc, $^{107}$Tc and $^{109}$Tc, the band with configura-

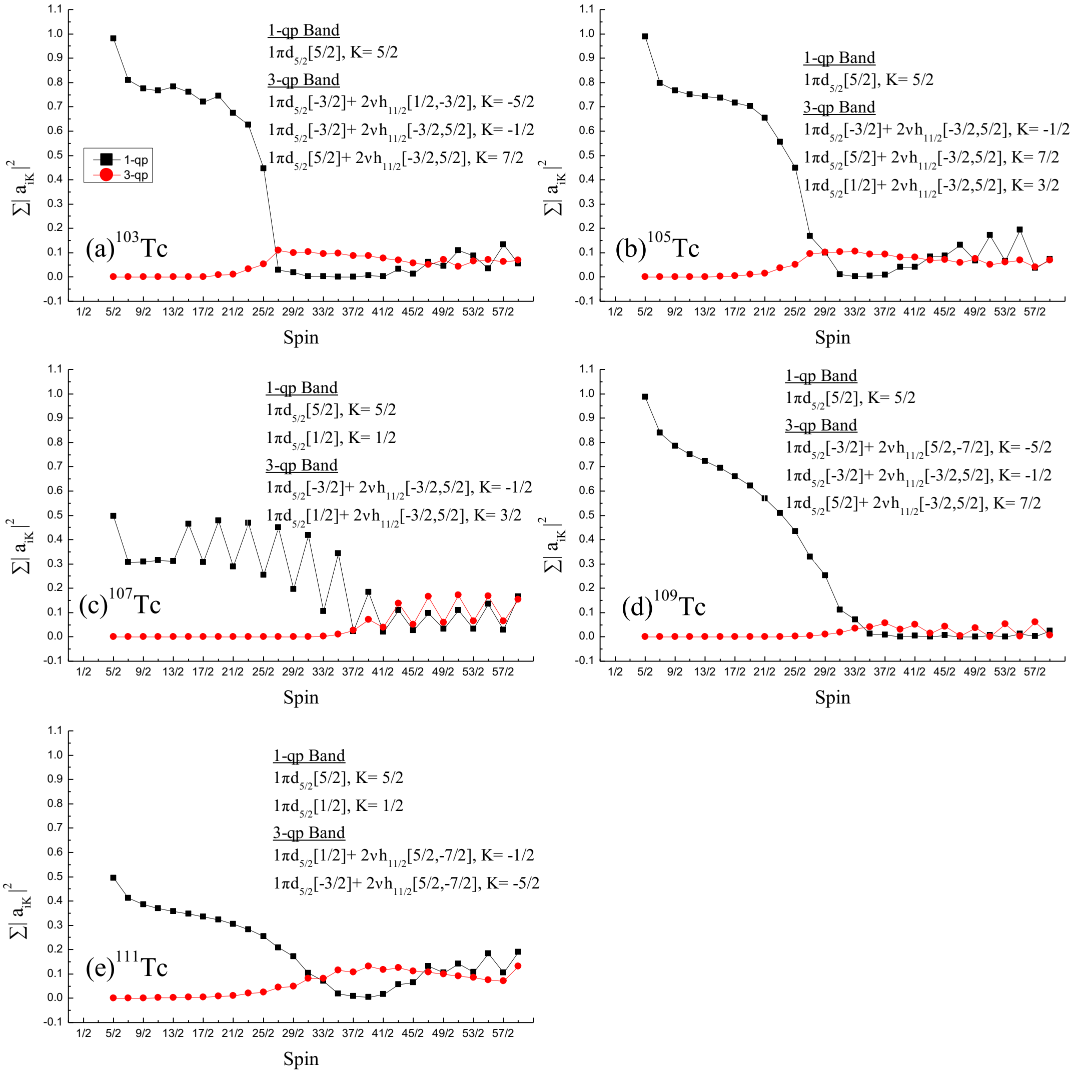

**Fig. 11.** Probability amplitude of various projected $K$-configurations in the wave functions of the yrast bands for (a) $^{103}$Tc, (b) $^{105}$Tc, (c) $^{107}$Tc, (d) $^{109}$Tc and (e) $^{111}$Tc.

tion $1\pi d_{5/2}$ $[-3/2] + 2\nu h_{11/2}$ $[-3/2, 5/2]$, $K = -1/2$ and in $^{111}$Tc, the band $1\pi d_{5/2}$ $[-3/2] + 2\nu h_{11/2}$ $[5/2, -7/2]$, $K = -5/2$ are found responsible for the occurrence of staggering, respectively.

### 3.2.4 Analysis of the wave function

Wave functions play a very important role in describing any nuclear structure quantity and these are used to explain the state of the nucleus. The probability amplitude of the wave function corresponding to the energy eigenvalues has been obtained by the diagonalization of the total Hamiltonian given in eq. (2). In figs. 11(a)–(e), the average of the amplitudes of the wave functions corresponding to various 1-*qp* and 3-*qp* bands, which are involved in the yrast band formation, are presented. One more thing that is quite clear from figs. 10(a)–(c) is that the mean of the amplitudes of the wave functions of 1-*qp* crosses the corresponding amplitude of 3-*qp* wave functions at those values of spin at which band crossing takes place (discussed in sect. 3.1). Further, the PSM results on back-bending (discussed in sect. 3.2.1) have also reported their occurrence at the same value of the spin at which crossing of wave function corresponding to 1-*qp* and 3-*qp* takes place. Thus, it can be concluded that the various nuclear structure quantities calculated in the present work using the PSM wave function arise due to combination of 1-*qp* and 3-*qp* wave functions.

## 4 Summary and perspectives

We have carried out a systematic study of the odd-$A$ Tc isotopes in the framework of the PSM for positive parity states and have investigated the effect of the inclusion $2d_{5/2}$ orbit in the valence space. It has been very effectively shown in the present PSM calculations that the presence of the $2d_{5/2}$ orbit is important for reproducing the energies of odd-$A$ $^{103-111}$Tc. In addition, a systematic study of the moment of inertia of these nuclei shows evidence for the effect of weakened pairing correlations due to the presence of deformed shell gaps. The calculated energy spectra and electromagnetic properties are in good agreement with the experimental data.

The authors would like to thank Prof. Y. Sun for providing the necessary support in carrying out the present piece of research.

## References

1. P. Moller, J.R. Nix, W.D. Myers, W.J. Swiatecki, At. Data Nucl. Data Tables **59**, 185 (1995).
2. J. Skalski, S. Mizutori, W. Nazarewicz, Nucl. Phys. A **617**, 282 (1997).
3. G.A. Lalazissis, S. Raman, P. Ring, At. Data Nucl. Data Tables **71**, 1 (1999).
4. A. Bharti, S.K. Khosa, Phys. Rev. C **53**, 2528 (1996).
5. A. Bauchet *et al.*, Eur. Phys. J. A **10**, 145 (2001).
6. J.K. Hwang *et al.*, Phys. Rev. C **57**, 2250 (1998).
7. Y.X. Luo *et al.*, Phys. Rev. C **70**, 044310 (2004).
8. J. Kurpeta *et al.*, Phys. Rev. C **86**, 044306 (2012).
9. W. Urban *et al.*, Eur. Phys. J. A **24**, 161 (2005).
10. Y.X. Luo *et al.*, Phys. Rev. C **74**, 024308 (2006).
11. M. Bernas *et al.*, Phys. Lett. B **331**, 19 (1994).
12. J. Kurpeta *et al.*, Phys. Rev. C **84**, 044304 (2011).
13. Y.X. Liu *et al.*, Nucl. Phys. A **858**, 11 (2011).
14. C. Sharma, P. Verma, S. Singh, A. Bharti, S.K. Khosa, Int. J. Mod. Phys. E **21**, 1250081 (2012).
15. A. Bhat, A. Bharti, S.K. Khosa, Int. J. Mod. Phys. E **21**, 1250030 (2012).
16. A. Bhat, A. Bharti, S.K. Khosa, Eur. Phys. J. A **48**, 39 (2012).
17. A. Kumar *et al.*, Int. J. Mod. Phys. E **24**, 1550076 (2015).
18. V. Velázquez, J.G. Hirsch, Y. Sun, Nucl. Phys. A **686**, 129 (2001).
19. K. Hara, Y. Sun, Nucl. Phys. A **537**, 77 (1992).
20. K. Hara, Y. Sun, Int. J. Mod. Phys. E **4**, 637 (1995).
21. Y. Sun, Phys. Scr. **91**, 043005 (2016).
22. S.G. Nilsson *et al.*, Nucl. Phys. A **131**, 1 (1969).
23. P. Ring, P. Schuck, *The Nuclear Many-Body Problem* (Springer, New York, 1980).
24. J.Y. Zhang, N. Xu, D.B. Fossan, Y. Liang, R. Ma, E.S. Paul, Phys. Rev. C **39**, 714 (1989).
25. D. De Frenne, Nucl. Data Sheets **110**, 1745 (2009).
26. J. Blachot, Nucl. Data Sheets **108**, 2035 (2007).
27. D. De Frenne, A. Negret, Nucl. Data Sheets **109**, 943 (2008).
28. J. Blachot, Nucl. Data Sheets **91**, 135 (2000).
29. G.G. Urdal, F.G. Kondev, Nucl. Data Sheets **113**, 1315 (2012).
30. L. Grodzin, Phys. Lett. **2**, 88 (1962).
31. H. Dejbakhsh, S. Shlomo, Phys. Rev. C **48**, 1695 (1993).
32. F. Iachello, A. Arima, *The Interacting Boson Model* (Cambridge University Press, Cambridge, 1987).
33. D. De Frenne, Nucl. Data Sheets **110**, 2081 (2009).
34. D. De Frenne, E. Jacobs, Nucl. Data Sheets **105**, 775 (2005).
35. J. Blachot, Nucl. Data Sheets **109**, 1383 (2008).
36. S. Kumar, J. Chen, F.G. Kondev, Nucl. Data Sheets **137**, 1 (2016).
37. J. Blachot, Nucl. Data Sheets **110**, 1239 (2009).
38. A. Ibáñnez-Sandoval, M.E. Ortiz, V. Velázquez, A. Galindo-Uribarri, P.O. Hess, Y. Sun, Phys. Rev. C **83**, 034308 (2011).
39. M. Sugawara *et al.*, Nucl. Phys. A **699**, 450 (2002).
40. N. Tajima, Nucl. Phys. A **572**, 365 (1994).